Investigation of metal distribution and carbide crystallite formation in metal-doped carbon films (a-C:Me, Me=Ti, V, Zr, W) with low metal content

Christoph Adelhelm[1*], Martin Balden[1], Marcin Rasinski[1,2], Stefan Lindig[1], Thomas Plocinski[2], Edmund Welter[3] and Marcin Sikora[4,5]

[1]Max-Planck-Institut für Plasmaphysik, Materials Research, EURATOM Association, Boltzmannstraße 2, 85748 Garching, Germany

[2]Faculty of Materials Science and Engineering, Warsaw University of Technology, ul. Wołoska 141, 02-507 Warsaw, Poland

[3]HASYLAB at Deutsches Elektronen-Synchrotron A Research Centre of the Helmholtz Association, Notkestr. 85, 22607 Hamburg, Germany

[4]European Synchrotron Radiation Facility, 6 rue Jules Horowitz, 38043 Grenoble, France

[5] Faculty of Physics and Applied Computer Science, AGH University of Science and Technology, Av. Mickiewicza 30, 30-059 Kraków, Poland

Dr. C. Adelhelm, Christoph.adelhelm@ipp.mpg.de Phone:+49-170-1550981 Fax: M. Balden

Dr. M. Balden, martin.balden@ipp.mpg.de Phone: +49-89-3299-1688 / -1212 (Fax)

M. Rasinksi, mrasin@o2.pl Tel: +48-22-234-8109 / -8750 (Fax)

S. Lindig, stefan.lindig@ipp.mpg.de Phone:+49-89-3299-1262 / -1212 (Fax)

Dr. T. Plocinski, tplocinski@inmat.pw.edu.pl Phone +48-22-234-8109 / -8750 (Fax)

Dr. E. Welter, edmund.welter@desy.de, +49-40-8998-4510 / -2787 (Fax)

Dr. M. Sikora, marcin.sikora@agh.edu.pl Phone: +48 12 6172304 / +48 12 6341247 (Fax)

[*] Corresponding author: C. Adelhelm (christoph.adelhelm@ipp.mpg.de)

Abstract

Metal-doped amorphous carbon films (a-C:Me) were produced at RT by magnetron sputtering using a metal (Me=Ti, V, Zr, W) and graphite target. The metal distribution and the temperature-induced carbide crystallite formation was analyzed by X-ray diffraction (XRD), electron microscopy (TEM, STEM) and X-ray absorption spectroscopy (EXAFS, XANES), focusing on low metal concentrations between 6.5 and 9.5 %. In as-deposited samples, the metal atoms are atomically distributed in the carbon matrix without significant formation of carbide particles. With annealing to 900 K the local atomic environment around the metal atoms becomes similar to the carbide. The carbide crystallites grow with annealing up to 1300 K, their size is depended on the metal type: $V>Ti>Zr\approx W$. W_2C and WC_{1-x} crystallites were identified for W-doped films, whereas the monocarbides are formed for the other metals. It is demonstrated, that EXAFS and high resolution electron microscopy are required to get a correct picture of the structure of the analyzed a-C:W films.

37 ## 1. Introduction

38 Metal-containing carbon films (a-C:Me, a-C:H:Me) were intensively studied in the last years
39 and have great importance for application as hard and wear resistant coatings. Most
40 frequently, the carbide forming metals Ti and W are used as dopants [1-7]. Improved
41 tribological and mechanical properties compared to pure carbon films are achieved by a
42 nanocomposite structure with nanometer-sized carbide particles in an amorphous matrix of
43 (hydrogenated) carbon. Such coatings are also investigated in respect to improved optical and
44 electrical properties [8, 9].

45 Our interest in a-C:Me films is motivated by research on the chemical sputtering process of
46 carbon by hydrogen impact [10]. This is of great importance for future fusion devices like
47 ITER, where carbon – together with Be and W – is suggested as plasma-facing material
48 (PFM) [11]. The reaction of hydrogen species with carbon-based PFM leads to its degradation
49 and to formation of undesired hydrocarbon layers, depositing in the reactor vessel [12]. If
50 radioactive tritium is used – together with deuterium the fuel for fusion – this leads to an
51 accumulating radioactive inventory, which is of high safety relevance. Doping of graphite
52 with carbide-forming transition metals (Ti, V, Zr, W) is a possible way to decrease its
53 reactivity against hydrogen species [10, 13, 14]. The presence of metals influence the erosion
54 mechanism, and accumulate at the surface as a result of preferential sputtering of carbon [15,
55 16]. For a systematic investigation of the effect of doping, erosion experiments have been
56 performed with metal-doped amorphous carbon films (a-C:Me), produced by dual source
57 magnetron sputter deposition. Their reactivity against hydrogen is determined by the kind of
58 metal and its concentration [17, 18], but depends also on the nano-structure of these layers
59 [19]. To study particularly the effect of the a-C:Me nanostructure on the erosion process, the
60 films were deposited at room temperature (RT) and annealed after deposition to induce
61 structural changes.

Therefore, our deposition conditions are in contrast to most publications dealing with characterization of a-C:Me films optimized for tribological applications. For those, the formation of a stable carbide phase in the carbon matrix already during deposition is desired, which requires high adatom mobility. This can be achieved either by increased substrate temperature or by a high energy of the impinging species (e.g. by using ion-beams [20], CVD/PVD hybrid deposition [21, 22], plasmas with higher ionization [23, 24], laser ablation [25]). A higher metal content is also beneficial for carbide phase formation [9, 26]. Also a sample bias is generally applied to increase the energy deposited in the growing film during deposition.

In contrast, this paper gives a detailed structural analysis of a-C:Me (Me=Ti, V, Zr, W) films with low metal content (1-19%) and the films were deposited at RT by non-reactive magnetron sputtering without bias. We focus on samples with 6.5-9.5 % metal content and describe the metal distribution after film deposition and the temperature-induced carbide cluster formation by annealing up to 1300 K. The following methods were used: X-ray diffraction (XRD), (scanning) transmission electron microscopy (TEM, STEM), and X-ray absorption fine structure spectroscopy (XAFS) in the extended energy (EXAFS) and near edge (XANES) region. The influence on the carbon structure was studied by Raman spectroscopy and XRD, and the results have been published in a separate paper [27]. A catalytic effect on the sp^2 clustering in the carbon phase during film deposition has been observed, which is dependent on the type of metal (W<V<Ti≈Zr).

2. Experimental

2.1 a-C:Me film deposition and composition

The a-C:Me films (Me = Ti, V, W, Zr) were deposited on Si (100) wafers by magnetron sputtering using a graphite and a metal cathode with argon as sputtering gas. The thickness

86 varied from about 0.7 to 1.5 µm. Details of the film preparation can be found elsewhere [27,
87 28]. The atomic film composition was determined by Rutherford backscattering spectroscopy
88 using a 3 MV tandem accelerator. All concentration values are given in at.%. After deposition
89 the samples were annealed at 700, 900, 1100 and 1300 K in high vacuum for 15 minutes.

90

91 **2.2 XRD**

92 The crystallographic phase and size of carbide crystallites formed in a-C:Me films were
93 determined by XRD using a Seifert XRD 3003 PTS diffractometer operated with Cu $K\alpha$
94 radiation. The experimental setup was optimized to measure thin films applying a parabolic
95 multilayer mirror on the primary side to achieve a parallel beam and almost complete $K\beta$
96 suppression. On the secondary side, a parallel plate collimator was installed to prevent
97 detection of non-parallel beam intensity. Diffractograms were acquired as theta-scans at a
98 fixed gracing incidence angle of 1°. For texture measurements the beam was restricted to 1
99 mm^2 at the primary side. Small samples ($\approx 5x5mm^2$) were mounted on Si wafers to exclude
100 contributions from the sample holder. The Scherrer formula with a pre-factor of 1 was used
101 for the estimation of the carbide crystallite size [29] under the assumption that peak
102 broadening is dominated by the small crystallite size. An experimental line width of about
103 0.3° was determined for the Si (111) peak at $2\theta = 28.4°$ for the used setup. Nevertheless, since
104 the observed peaks are generally much broader, its influence on the crystallite size
105 determination was neglected. The peak FWHM was obtained by fitting PearsonVII profiles to
106 the partly overlapping (100) and (111) diffraction peaks using the program fityk (0.7.6) [30],
107 including a linear background. Error bars were derived from the uncertainty introduced by the
108 fitting procedure.

109

110 **2.3 Microscopy**

111 For TEM analysis a set of samples of annealed a-C:V and a-C:Ti films on silicon wafers were
112 prepared by ion polishing and analyzed with a Philips EM 430 operated at 300 kV. Estimation
113 of the average carbide crystallite size was performed by analyzing about 200-400 particles,
114 giving the average diameter with standard deviation. A focused ion beam microscope (FIB)
115 was used for the preparation of a thin lamella of 6.5% and 9.5 % a-C:W samples. Argon ion
116 milling in a Gentle Mill device was applied for final thinning and elimination of defects
117 introduced by FIB. STEM observation was carried out on a 200 kV UHR STEM microscope
118 (Hitachi HD-2700) equipped with a C_s corrector. Nano diffraction with the STEM was
119 applied for single crystal phase analysis.

120

121 **2.4 XAFS measurements**

122 XAFS measurements at the *K* absorption edges of Ti, V and Zr as well as the W *L3*-edge were
123 performed at HASYLAB (Hamburg) on beamline C. XAFS spectra of a-C:Me films were
124 acquired in fluorescence yield mode using a 7 channel HPGe-detector (Canberra, Olen,
125 Belgium) perpendicular to the incident X-ray. A Si (111) double crystal monochromator was
126 used at the Ti and V edge, a Si (311) crystal was applied for Zr and W. All measurements
127 were performed at room temperature.

128 For measurement of pure carbides (as powders, W_2C as sintered particle) total electron yield
129 detection was applied. The measured energy range was about -200 eV to +800 eV in respect
130 to the used absorption edge of the metal. The software ATHENA [31] was used for data
131 analysis and extraction of the EXAFS data.

132 The W *L1*-edge measurements limited to the edge-near region (i.e. XANES) were performed
133 at beamline ID26 of ESRF (Grenoble). A Si (311) double crystal monochromator was applied

134 to collect high resolution XANES spectra at the maximum of the W $L_{\beta 3}$ emission line (9819

135 eV), detected by a spectrometer consisting of a Si (660) analyzer crystal and an avalanche

136 photodiode. The spectra were measured from 12080-12150 eV incident photon energy and

137 normalized to the edge step at the highest energy.

138 ## 3. Results

139 For this study, a-C:Me films (Me = Ti, V, Zr, and W) with metal concentrations from 1 up to
140 19 % were investigated by XRD, TEM/STEM and X-ray absorption techniques. The
141 presented results are focused on carbon films with similar metal concentrations, ranging from
142 6.5 to 9.5 %. If different results are obtained for lower (1-3.5 %) or higher (up to 11-19 %)
143 concentrations, it will be noted.

144

145 ### 3.1 XRD and electron microscopy

146 3.1.1 Ti, V and Zr-doped films

147 The X-ray diffractograms for an annealing series of a 7.5% a-C:Ti film are shown in Fig. 1a.
148 For the as-deposited and 700 K annealed samples no indication for TiC formation can be
149 observed from the diffractograms. In a recent study by Lewin et al. [9] a 12 % Ti containing
150 a-C:Ti film also remained X-ray amorphous. The weak bump around 43° is due to scattering
151 from the carbon phase [27]. Annealing to 900 K and higher leads to occurrence of peaks
152 which can be attributed to the (111) and (200) reflection of TiC. A similar picture was
153 observed for a 8.5 % V containing film (Fig. 1b).

154 The diffraction patterns of the 7 % a-C:Zr film are depicted in Fig. 1c. A broad bump around
155 31° occurs already for the as-deposited sample. After annealing to 900 K a slight increase in
156 intensity and a shift of the maximum to 32° can be observed. For 1100 K the diffraction
157 pattern exhibits signals which can be attributed to the (111) peak with a shoulder referring to
158 (200), and the (220) reflection of ZrC. For 1300 K, all three ZrC peaks are clearly developed.

159 The formed carbide particles are in the nanometer range as shown in Fig. 2 for a-C:V films,
160 where the VC crystallite sizes are presented for 4 different metal concentrations, calculated by
161 using the Scherrer formula. A clear carbide signature below 900 K was only visible for the

162 19% V containing film. Generally, the carbide particle size in a a-C:V film of a given
163 concentration is increasing with the annealing temperature. After annealing to 1300 K the
164 crystallite size is inversely proportional to the V concentration in the film. Evaluation of the
165 crystallite size was also done by TEM for 3 specimens, confirming the size determined by
166 XRD (Fig. 2). A TEM micrograph of the 1.5 % a-C:V sample annealed to 1300 K is presented
167 in Fig. 3. It clearly shows that the carbide particles have a broad size distribution, which is
168 reflected in the large standard deviation of the crystallite size determined by TEM (Fig. 2).

169 Fig. 4 summarizes carbide particle sizes derived from XRD for Ti, V, and Zr-doped films
170 annealed from 900 up to 1300 K. From this graph the influence of the metal type on the
171 particle size can be observed. For the 1300 K data, no overlap between the different dopants
172 occurs, showing best the general trend in crystallite size: ZrC < TiC < VC. An explanation for
173 this sequence can be given by comparing the carbide melting temperatures, which can be
174 regarded as a measure for the carbide crystallite stability: ZrC (3693 K) > TiC (3340 K) > VC
175 (3103 K) [32]. The lower the carbide crystal stability, the lower the temperature at which
176 metal atoms can leave the surface of a carbide particle to diffuse to another particle, which
177 gains in size (Ostwald ripening process).

178

179 3.1.2 a-C:W

180 Fig. 5 shows the evolution of the diffraction patterns of a 9.5% a-C:W film. Even without
181 annealing an intensive, broad peak can be observed around 37.4°. With annealing, the peak
182 maximum shifts slightly to higher angles (38.6° for 1300 K), becomes more intensive and
183 decreases in width. The FWHM reduces from 11.3° (as-deposited) to 6.1° (1300 K). Two
184 other peaks can be separated at 62 and 75° for annealing to ≥ 1100 K.

185 Similar spectra were observed for a 6.5% a-C:W film; only the intensities in the
186 diffractograms of the broad peaks are lower.

187 The broad diffraction peak around 37° is well known for C-W films and reported in earlier
188 publications [8, 20, 22, 23, 25, 33]. It is generally explained by the formation of very small
189 WC_{1-x} crystallites with preferred (111) orientation and high degree of disorder/amorphization.
190 However, to our knowledge, no proof of the texture by pool figure analysis has been
191 published. Also, unambiguous diffraction rings in TEM are often found for high energy
192 deposition and/or higher W concentrations [6, 20, 22]. The maximum of the peak for the
193 diffractogram after deposition fits to the (111) peak of WC_{1-x} at 37°, and the maximum for
194 1300 K coincides with the (002) reflection of W_2C. However, since a) no other peaks can be
195 used to verify the phase and b) both peaks are not the most intensive for each carbide phase,
196 no assignment of a tungsten carbide phase was done on the basis of our XRD data. Texture
197 analysis on the nominal angles of diffraction peaks of WC, W_2C and WC_{1-x} confirm
198 unambiguously that the missing appearance of further peaks due to strong texture can be
199 excluded. An influence of changes in the film stress state during annealing on the observed
200 shift of the peak at 37° can be excluded: The calculated stress would be in the order of 15 GPa
201 which cannot not be accommodated in the film.

202 As described above, the unambiguous identification of a crystallographic phase in the a-C:W
203 sample is not possible by XRD. Therefore, no evaluation by the Scherrer formula was
204 performed, and no data for a-C:W is included in Fig. 4. By conventional TEM analysis, no
205 crystalline carbide particles could be detected even in annealed a-C:W films (only diffuse
206 dark spots were observed for 1300 K annealed samples). High resolution STEM analysis
207 showed also no crystalline carbide particles in the as-deposited 9.5 % a-C:W sample.
208 However, for the 1300 K annealed specimen, small carbide particles with a diameter of up to
209 3 nm could be observed (Fig. 6a). Fig. 6b shows the same area in the Z contrast mode. Here,
210 regions enriched in W appear bright, carbon appears dark. It shows also W-rich regions with
211 clusters sizes in the order of 1 nm.

212 Local nano diffraction of single particles revealed the presence of the W_2C as well as the
213 WC_{1-x} phase. From 9 analyzed particles, 5 were labeled as WC_{1-x} and 4 as W_2C. A 1300 K
214 annealed 6.5 % a-C:W sample showed also both phases and similar particle sizes.

215

216 **3.2 XAFS**

217 In contrast to XRD and TEM analysis, XAFS analysis does not require a crystalline phase. It
218 is a local atomic probe, and only the atomic environment in a few Å distance around the metal
219 atom contributes to the signal [34].

220

221 3.2.1 a-C:Ti and a-C:V

222 Fig. 7a shows XAFS spectra of the 7.5 % a-C:Ti sample, annealed up to 1300 K, as well as
223 the spectrum of a TiC standard. The spectra of the as-deposited and 700 K annealed samples
224 show only one broad bump after the edge. After annealing to 900 K the signal is more
225 structured and for higher temperatures the spectra correspond to the spectrum of the TiC
226 standard.

227 The XANES region is shown in Fig. 7b. The absorption edge shifts to higher energy with
228 increasing annealing temperature; for the 1300 K annealed sample the edge position
229 corresponds to that of the TiC standard. This trend is probably related to a better Ti-C
230 bonding with increased electron transfer from Ti to C. The position of the first peak above the
231 absorption edge does not vary, but slightly increases in intensity with annealing. The pre-edge
232 region is magnified in the inset of Fig. 7b. It shows that the pre-edge part around 4968 eV
233 decreases in intensity with annealing temperature, indicating a change in symmetry [35].

234 Fig. 8 shows the EXAFS data after Fourier transformation (k=2-8.5 $Å^{-1}$). In this
235 representation, the EXAFS is plotted in radial distance to the Ti atom. The data is not

236 corrected for the phase shift, therefore the R gives no real atomic distances. A first neighbor
237 peak is present around R=1.5 Å. This first shell corresponds to carbon atoms, and no defined
238 second shell from a Ti next neighbor (as in TiC) occurs. However, a shoulder at the higher R
239 side can be observed which gains intensity for the 700 K sample. With annealing to 900 K,
240 the second peak at 2.4 Å – corresponding to the second shell (Ti-Ti) – is well developed. For
241 900 K and higher temperatures, the local atomic environment of Ti is identical to TiC.

242 EXAFS data after Fourier transformation for as-deposited a-C:Ti films with different
243 concentrations are shown in Fig. 9. For 1 % Ti, an intensive peak at lower R compared to the
244 7.5 % film occurs. For the 13 % a-C:Ti film, the Ti shell is visible. The intensive peak for 1%
245 Ti could be attributed to the formation of a first shell consisting of O atoms (an oxygen
246 concentration of about 2 % was determined by RBS). The Ti-O distance (1.93-1.96 Å) is
247 shorter than the Ti-C distance (2.16 Å). In addition, the Ti edge energy position of the 1 % a-
248 C:Ti film is higher than for all other as-deposited a-C:Ti films (e.g. 1.2 eV higher as for the
249 7.5 % Ti doped film). This can be explained by the more polar Ti-O bond and a more
250 pronounced electron transfer from Ti to O compared to C. Annealing of the 1 % a-C:Ti
251 sample up to 1100 K leads to an increasing intensity of the oxygen peak, but not to formation
252 of TiO_2 crystallites. After annealing to 1300 K, the local environment changed and became
253 similar to TiC. This sample showed no TiC diffraction peaks in XRD.

254 In general, the 8.5 % a-C:V EXAFS data shows a similar development for the annealing
255 series, as obvious from Fig. 10a. No indication for an oxygen first shell can be observed for
256 the as-deposited sample of 1.5 % V (Fig. 10b). The 19 % a-C:V film shows a VC-like local
257 environment already after deposition which is confirmed by carbide peaks in XRD.

258

259 3.2.2 a-C:Zr and a-C:W

260 The as-deposited carbon films with 7 % Zr and especially the 9.5 % W show broad peaks in
261 the X-ray diffractograms (Fig. 1c, Fig. 5). However, the EXAFS measurements show that
262 carbide crystallites are only present in annealed samples: Fig. 11a presents EXAFS data for
263 the Zr-doped sample after deposition and annealing to 900 and 1100 K. Only after annealing
264 to 1100 K, the signal becomes similar to the ZrC standard. However, the signal intensity of
265 the a-C:Zr film is lower, which is probably due to the small particle size and the use of
266 electron yield detection for the ZrC standard. To show the influence of the second next
267 neighbor of Zr on the EXAFS signal, Fig. 11b gives $|\chi(k)|$ of the as-deposited sample and the
268 backtransformed data for R = 1.1-2.1 Å (data range of the first shell) and R = 1.1-3.5 Å (data
269 range of the first and second shell). $|\chi(k)|$ is mainly determined by scattering at the first
270 neighbor; however, including the second shell (R=1.1-3.35 Å) slightly improves the
271 description of $|\chi(k)|$ between k=6-8.5 $Å^{-1}$.

272 In Fig. 12a EXAFS data is presented for the 9.5% a-C:W sample and a W_2C standard. Only a
273 first neighbor peak is observed for the as-deposited sample. Annealing up to 900 K only
274 slightly changes $|\chi(R)|$. For the 1300 K annealed sample the signal becomes similar to the
275 W_2C standard for the first and second shell (R = 1-3.5 Å). However, the intensity is not fully
276 reproduced and diminishes for R > 4 Å. Since STEM analysis showed the presence of W_2C
277 and WC_{1-x} phase it is clear, that the EXAFS (which is an average over all W atoms) does not
278 fully correspond to the W_2C standard spectrum. As obvious from Fig. 12b, no significant
279 contribution of a second shell contributes to $|\chi(k)|$ for the as-deposited sample.

280 EXAFS spectra for 14.5 % gave comparable results. For the 2.5 and 4 % W containing films,
281 the second shell is not well developed even after annealing at 1300 K.

282 The XANES region of the spectra acquired at the W L_3 edge is not very sensitive to the local
283 electronic structure: the edge region is dominated by a strong white line due to transitions into
284 almost empty 5d levels. In addition to EXAFS measurements, XANES measurements of a-

285 C:W films at the W L_1 edge were performed to compare the local electronic environment of
286 W in W-doped films with different W standard materials. Fig. 13 compares XANES spectra
287 of W, W_2C, WC and WC_{1-x} [33, 36] with the spectra of a 6.5% a-C:W film (as-dep., 900 K,
288 1300 K). It reveals significant difference of the shape and energy position of the reference
289 spectra, which are the fingerprints of the local symmetry, coordination, and valence of the
290 probed atom species [35]. The W_2C, WC_{1-x} and WC spectra show a gradual shape evolution.
291 Upon increasing W/C ratio the edge energy shifts towards lower energy.

292 The spectra of as-deposited and annealed samples are not identical, showing a clear difference
293 especially in the pre-edge intensity. A gradual decrease of the pre-edge peak intensity with
294 increasing the annealing temperature is observed, which is attributed to the enhancement of
295 the average local symmetry around the W atoms upon annealing [37]. The spectrum of the
296 1300 K annealed 6.5% a-C:W film is more similar to that of the W_2C reference than to that of
297 WC_{1-x}.

298 ## 4. Discussion

299 The absence of a second shell (metal-metal) peak in the EXAFS data clearly shows that the
300 metal atoms are distributed atomically disperse in the carbon matrix in as-deposited samples,
301 surrounded by a carbon first shell. No significant carbide particle formation has occurred
302 (except 19 % V). This finding is independent from the metal type. For 1 % Ti, a Ti-O first
303 shell was proposed (Fig. 9). The results are related to the low metal content and especially the
304 soft deposition conditions used in our preparation process (RT, no bias). Other publications
305 dealing with the structural investigation of a-C:Me films report the formation of carbide
306 crystallites even for lower [20, 21] or similar concentrations [38]. This can be attributed to the
307 higher energies of the impinging species in these depositions (unbalanced magnetron, ion
308 beam deposition). Also, significantly higher metal concentrations are used in most studies.

309 With annealing, carbide particle formation occurred in all samples, which is evident from the
310 EXAFS data, but also from XRD. After annealing to 1300 K, the largest crystallites were
311 observed for V-doping, the smallest particles were observed in Zr (Fig. 4) and W-doped films
312 (Fig. 6). The relatively low melting point of the tungsten carbides (below 3100 K [39]) does
313 not fit to the above mentioned inverse relation between melting point and carbide crystallite
314 size for VC, Ti, ZrC. A possible explanation is, that the particle growth is not only limited by
315 the binding energy of the metal atoms in a carbide crystallite, but also by the diffusion in the
316 carbon matrix, which is the lowest for W due to its high atomic mass.

317 The X-ray diffractograms of as-deposited samples containing Zr and W (Fig. 1c and 5) show
318 broad peaks, especially for W. As mentioned above, similar spectra are often found for C
319 films containing W [8, 20, 22, 23, 25, 33] and are generally interpreted in a way that textured
320 WC_{1-x} nanoparticles have been formed. However, our EXAFS analysis reveals that this
321 interpretation does not correctly describe the structural situation in our a-C:W films: The
322 majority of the W atoms is dispersed in the carbon matrix and not present in a carbide

323 particle. In addition, high resolution STEM analysis showed carbide particles only after
324 annealing. For 1300 K, both W_2C and WC_{1-x} crystallites are present. This is also not reflected
325 in the XRD pattern in Fig. 5. Still, only a single peak is present between 2θ = 30-50°.
326 Therefore, the X-ray diffractogram of the 1300 K annealed sample is at least a result of
327 different crystallographic phases and small crystallite size. The texture analysis showed that
328 the tungsten carbide particles have no preferred orientation. Therefore, a possible texture of
329 the crystallites is not responsible for the missing peaks compared to the pure carbides. In
330 addition, scattering from a small amount of W-C clusters below 1 nm with possible high
331 distortion could contribute to the diffraction pattern. This would also be an explanation for the
332 spectrum of the as-deposited a-C:W film. However, only a minor fraction of W atoms can be
333 located in such clusters, because from the EXAFS results significant clustering of W atoms
334 can be excluded. The combination of XRD, STEM and EXAFS analysis shows that the
335 occurance of the broad XRD peak around 37° does not always correspond to a carbon film
336 containing WC_{1-x} crystallites.

337 For 3d transition metals, large pre-edge peaks in the XANES spectra are observed in low
338 symmetry coordination while their intensity almost diminishes in structures characterized by
339 inversion symmetry [35]. Therefore, the pre-edge intensity can be considered as an indication
340 of local distortion. In the XANES spectra of the as-deposited 7.5 % a-C:Ti (Fig. 7b), a lower
341 coordination number and high distortion around the Ti atom could explain the higher pre-edge
342 peak intensity compared to TiC. With annealing, a higher symmetry is achieved due to
343 increasing order and the formation and growth of TiC crystallites. This is also reflected in the
344 shift of the edge position to higher energies, due to increased electron transfer from Ti to C.
345 For the 6.5 % a-C:W sample, the W L_1 XANES pre-edge also shows a decrease in intensity
346 with annealing. On the other hand, no significant shift in the edge position is observed. The
347 XANES of the 1300 K annealed sample is more similar to the W_2C standard than WC_{1-x}.
348 However, STEM analysis clearly showed the occurrence of both phases. A XANES spectrum

is a result of all probed atoms and strongly depends on distortion, crystallographic phase and crystallite size. Therefore, XANES analysis could not be applied for phase determination in the investigated a-C:W films.

5. Summary

In as-deposited a-C:Me films (Me=Ti, V, Zr) with low metal concentrations no carbide particles could be observed after deposition, and the metal atoms are distributed atomically disperse in the carbon matrix under the here applied deposition conditions. The local atomic environment around the metal atoms was probed by EXAFS and becomes similar to the pure carbides after annealing to 900 K (Ti and V) or 1100 K (Zr). Samples annealed to 900 K and higher showed also carbide peaks in XRD. The carbide particle size depends on the metal species: V>Ti>Zr.

For W-doped films, broad peaks can be observed in the X-ray diffractograms already after deposition. However, EXAFS clearly shows that no significant carbide clustering is present in the samples. STEM analysis revealed up to 3 nm large WC_{1-x} and W_2C particles in samples annealed to 1300 K. This information cannot be deduced from the XRD data, and shows that relying only on XRD can lead to wrong conclusions for a-C:W films.

Acknowledgement

The research leading to these results has received funding from the European Atomic Energy Community's Seventh Framework Program (FP7 / 2007-2011) under Grant Agreement No 224752. We acknowledge ESRF and HASYLAB for the provision of beam time and the ID26 staff for help in setting up the experiment.

372 ## References

373

374 1. Voevodin, A.A., S.V. Prasad, and J.S. Zabinski, *Nanocrystalline carbide amorphous*
375 *carbon composites.* Journal Of Applied Physics, 1997. **82**(2): p. 855-858.
376 2. Meng, W.J. and B.A. Gillispie, *Mechanical properties of Ti-containing and W-*
377 *containing diamond-like carbon coatings.* Journal of Applied Physics, 1998. **84**(8): p.
378 4314-4321.
379 3. Stüber, M., et al., *Microstructure and properties of low friction TiC-C nanocomposite*
380 *coatings deposited by magnetron sputtering.* Surface & Coatings Technology, 2002.
381 **150**(2-3): p. 218-226.
382 4. Nilsson, D., et al., *Low-friction carbon-rich carbide coatings deposited by co-*
383 *sputtering.* Wear, 2003. **254**(11): p. 1084-1091.
384 5. Pei, Y.T., D. Galvan, and J.T.M. De Hosson, *Nanostructure and properties of TiC/a-C*
385 *: H composite coatings.* Acta Materialia, 2005. **53**(17): p. 4505-4521.
386 6. Abad, M.D., et al., *Tailored synthesis of nanostructured WC/a-C coatings by dual*
387 *magnetron sputtering.* Surface & Coatings Technology, 2010. **204**(21-22): p. 3490-
388 3500.
389 7. Sanchez-Lopez, J.C., et al., *Metal carbide/amorphous C-based nanocomposite*
390 *coatings for tribological applications.* Surface & Coatings Technology, 2009. **204**(6-
391 7): p. 947-954.
392 8. Abad, M.D., et al., *WC/a-C nanocomposite thin films: Optical and electrical*
393 *properties.* Journal of Applied Physics, 2009. **105**(3): p. 033510.
394 9. Lewin, E., O. Wilhelmsson, and U. Jansson, *Nanocomposite nc-TiC/a-C thin films for*
395 *electrical contact applications.* Journal of Applied Physics, 2006. **100**(5): p. 054303-
396 10.

397 10. Jacob, W. and J. Roth, *Chemical Sputtering* in *Sputtering by Particle Bombardment.*
398 *Experiments and Computer Calculations from Threshold to MeV Energies*, R.
399 Behrisch and W. Eckstein, Editors. 2007, Springer: Berlin.
400 11. Barabash, V., et al., *Materials challenges for ITER - Current status and future*
401 *activities.* Journal of Nuclear Materials, 2007. **367-370**(Part 1): p. 21-32.
402 12. Roth, J., et al., *Recent analysis of key plasma wall interactions issues for ITER.*
403 Journal of Nuclear Materials, 2009. **390-91**: p. 1-9.
404 13. Balden, M., et al., *Chemical erosion of carbon doped with different fine-grain*
405 *carbides.* Journal Of Nuclear Materials, 2001. **290**: p. 52-56.
406 14. Pardo, E.d.J., et al., *Erosion Processes of Carbon Materials under Hydrogen*
407 *Bombardement and their Mitigation by Doping.* Physica Scripta, 2004. **T111**: p. 62-
408 67.
409 15. Balden, M., *Overview on the effects of dopants on chemical erosion and RES of*
410 *carbon-based materials.* Physica Scripta, 1999. **T81**: p. 64-69.
411 16. Salonen, E., et al., *Reduced chemical sputtering of carbon by silicon doping.* Journal
412 of Applied Physics, 2002. **92**(4): p. 2216-2218.
413 17. Balden, M., et al., *Deuterium-induced chemical erosion of carbon-metal layers.*
414 Journal of Nuclear Materials, 2005. **337-39**(1-3): p. 980-984.
415 18. Balden, M. and C. Adelhelm, *Characterization and erosion of metal-containing*
416 *carbon films.* Physica Scripta, 2007. **T128**: p. 121-126.
417 19. Starke, P., C. Adelhelm, and M. Balden, *Erosion behaviour of metal-doped carbon*
418 *layers in deuterium low pressure plasmas and the determination by optical emission*
419 *spectroscopy.* Contributions to Plasma Physics, 2007. **47**(7): p. 530-536.
420 20. Wang, A.Y., et al., *Structure and mechanical properties of W incorporated diamond-*
421 *like carbon films prepared by a hybrid ion beam deposition technique.* Carbon, 2006.
422 **44**(9): p. 1826-1832.

423 21. Meng, W.J., R.C. Tittsworth, and L.E. Rehn, *Mechanical properties and*
424 *microstructure of TiC/amorphous hydrocarbon nanocomposite coatings.* Thin Solid
425 Films, 2000. **377**: p. 222-232.
426 22. Park, S.J., et al., *Microstructure and mechanical properties of WC-C nanocomposite*
427 *films.* Diamond and Related Materials, 2002. **11**(10): p. 1747-1752.
428 23. Kao, W.H., *Optimized a-C : W-x% coatings with enhanced tribological properties and*
429 *improved micro-drilling performance.* Surface & Coatings Technology, 2007. **201**(16-
430 17): p. 7392-7400.
431 24. Pei, Y.T., et al., *Microstructural control of TiC/a-C nanocomposite coatings with*
432 *pulsed magnetron sputtering.* Acta Materialia, 2008. **56**(4): p. 696-709.
433 25. Voevodin, A.A., et al., *Nanocrystalline WC and WC/a-C composite coatings produced*
434 *from intersected plasma fluxes at low deposition temperatures.* Journal of Vacuum
435 Science & Technology A, 1999. **17**(3): p. 986-992.
436 26. Meng, W.J., et al., *Ti atomic bonding environment in Ti-containing hydrocarbon*
437 *coatings.* Journal of Applied Physics, 2000. **88**(5): p. 2415-2422.
438 27. Adelhelm, C., et al., *Influence of doping (Ti, V, Zr, W) and annealing on the sp[sup 2]*
439 *carbon structure of amorphous carbon films.* Journal of Applied Physics, 2009.
440 **105**(3): p. 033522-9.
441 28. Balden, M., et al., *Metal-doped carbon films obtained by magnetron sputtering.*
442 Surface and Coatings Technology, 2005. **200**(1-4): p. 413-417.
443 29. Birkholz, M., *Thin Film Analysis by X-Ray Scattering*. 2006, Weinheim: Wiley-VCH
444 30. http://www.unipress.waw.pl/fityk/.
445 31. Ravel, B. and M. Newville, *ATHENA, ARTEMIS, HEPHAESTUS: data analysis for X-*
446 *ray absorption spectroscopy using IFEFFIT.* Journal of Synchrotron Radiation, 2005.
447 **12**: p. 537-541.
448 32. Pierson, H.O., *Handbook of Refractory Carbides and Nitrides*

449 *Properties, Characteristics, Processing and Applications*. Materials Science and
450 Process Technology Series. 1996, Westwood: Noyes. 340.
451 33. Schiffmann, K.I., et al., *Sizes and distances of metal clusters in Au-, Pt-, W- and Fe-*
452 *containing diamond-like carbon hard coatings: a comparative study by small angle X-*
453 *ray scattering, wide angle X-ray diffraction, transmission electron microscopy and*
454 *scanning tunnelling microscopy.* Thin Solid Films, 1999. **347**(1-2): p. 60-71.
455 34. Koningsberger, D.C. and R. Prins, *X-Ray Absorption. Principles, Applications,*
456 *Techniques of EXAFS, SEXAFS and XANES*. Chemical Analyis, ed. W. J.D. Vol. 92.
457 1988, New York: John Wiley & Sons.
458 35. Yamamoto, T., *Assignment of pre-edge peaks in K-edge x-ray absorption spectra of*
459 *3d transition metal compounds: electric dipole or quadrupole?* X-Ray Spectrometry,
460 2008. **37**(6): p. 572-584.
461 36. The WC1-x thin film sample was received by K. Schiffmann, Fraunhofer Institut für
462 Schicht- und Oberflächentechnik, Braunschweig, Germany. XRD data of this sample
463 (55 % W) is published in [33].
464 37. Yamazoe, S., et al., *XAFS study of tungsten L-1- and L-3-edges: Structural analysis of*
465 *WO3 species loaded on TiO2 as a catalyst for photo-oxidation of NH3.* Journal of
466 Physical Chemistry C, 2008. **112**(17): p. 6869-6879.
467 38. Feng, B., et al., *Characterization of microstructure and mechanical behavior of*
468 *sputter deposited Ti-containing amorphous carbon coatings.* Surface & Coatings
469 Technology, 2001. **148**(2-3): p. 153-162.
470 39. Kurlov, A. and A. Gusev, *Tungsten carbides and W-C phase diagram.* Inorganic
471 Materials, 2006. **42**(2): p. 121-127.
472
473

474 Fig. 1

475

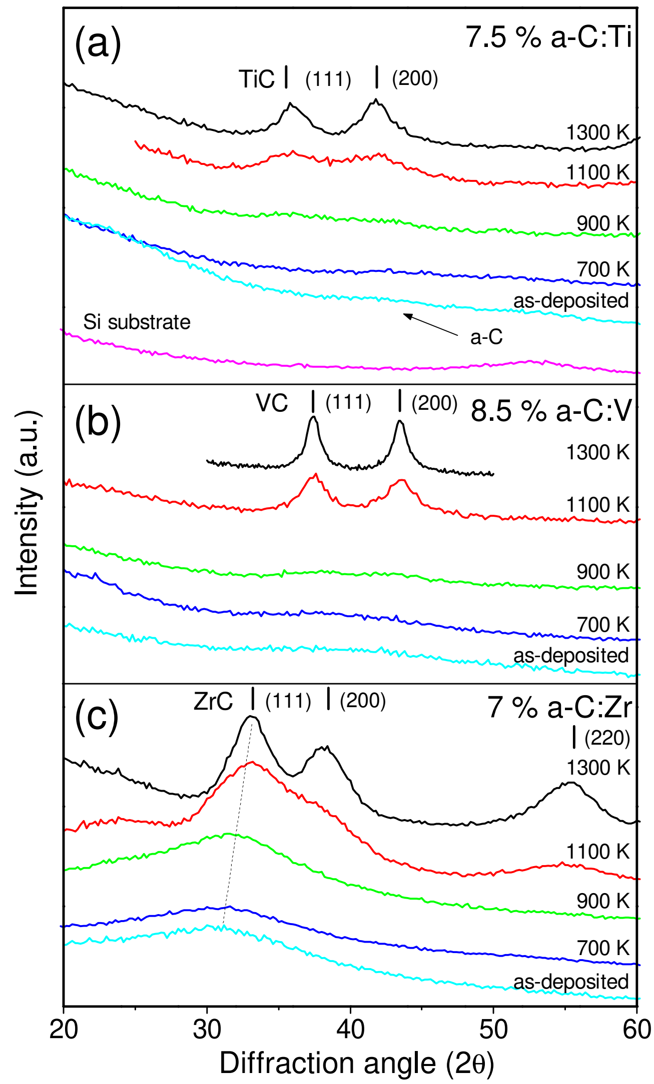

476

477 Fig. 2

478

479

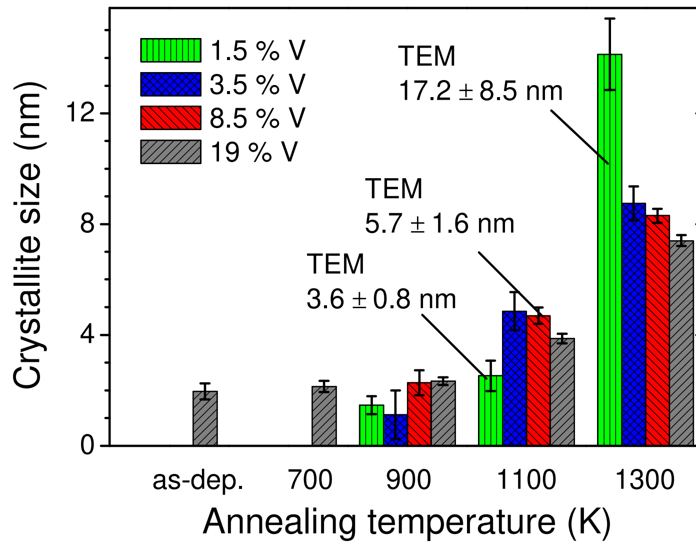

480

481 Fig. 3

482

483

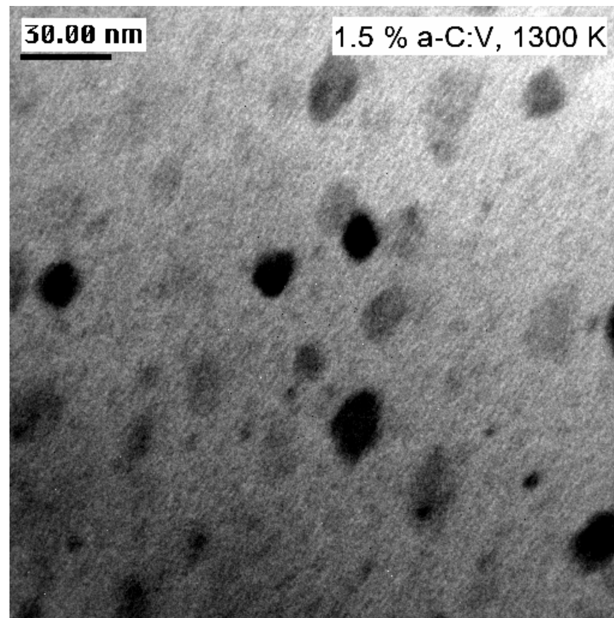

484

485 Fig.. 4

486

487

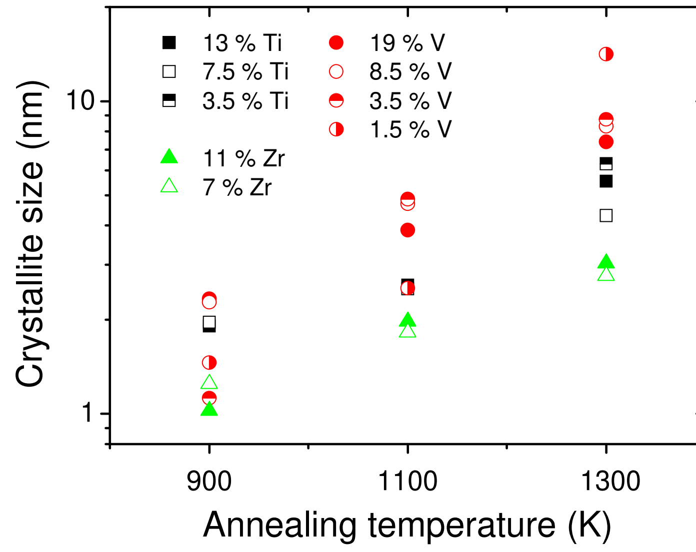

488

489 Fig. 5

490

491

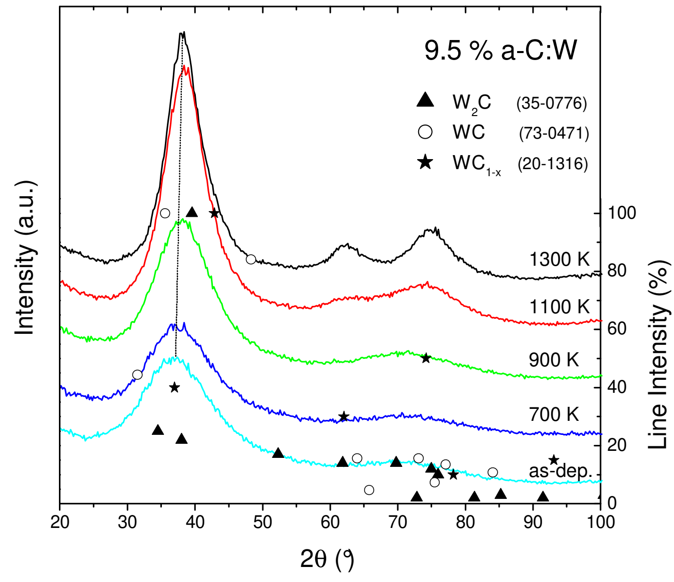

492

493 Fig. 6

494

495

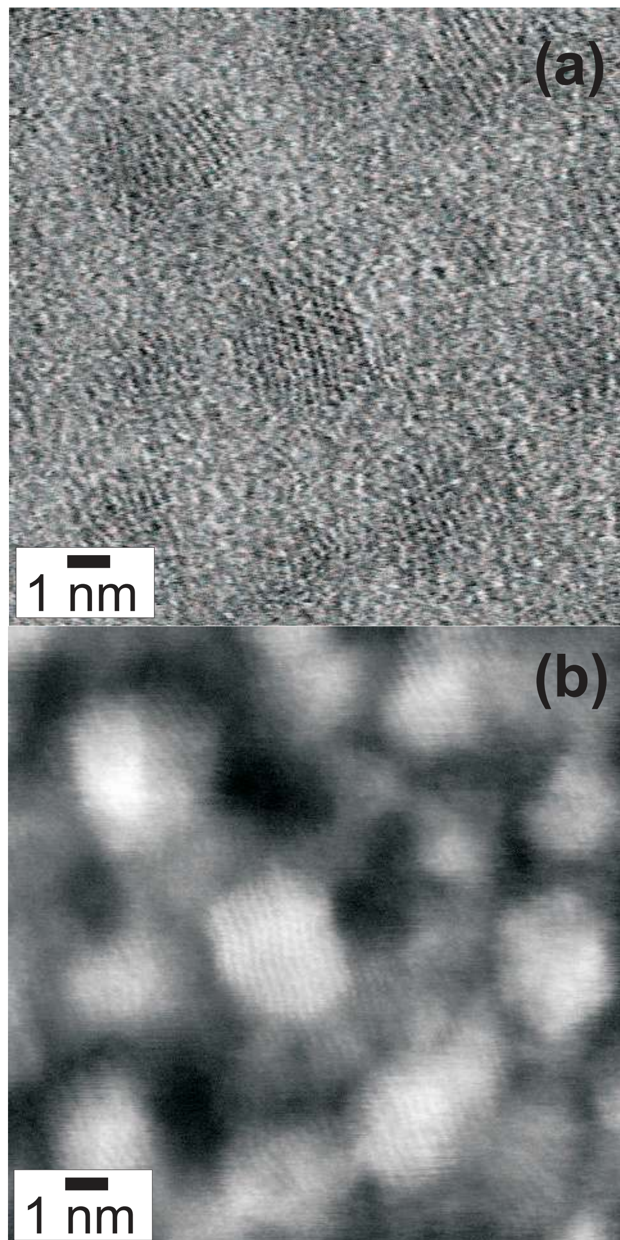

496

497

498 Fig. 7

499

500

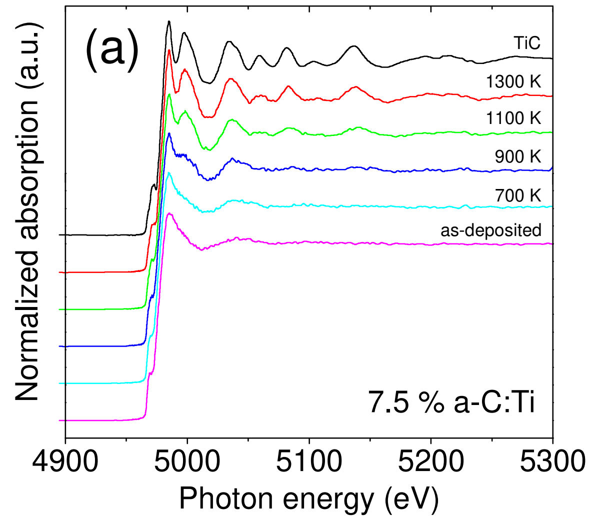

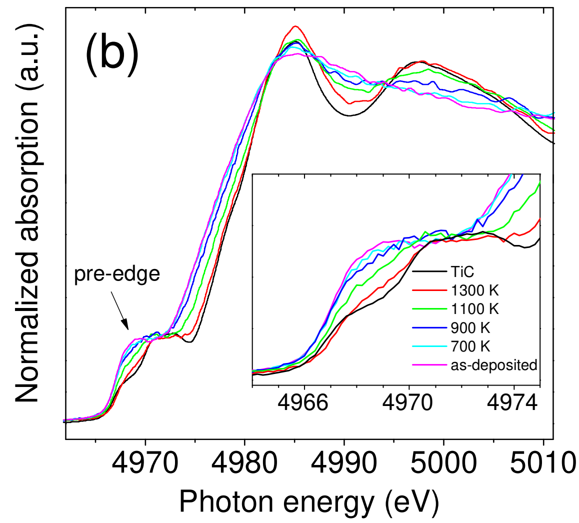

501

502 Fig. 8

503

504

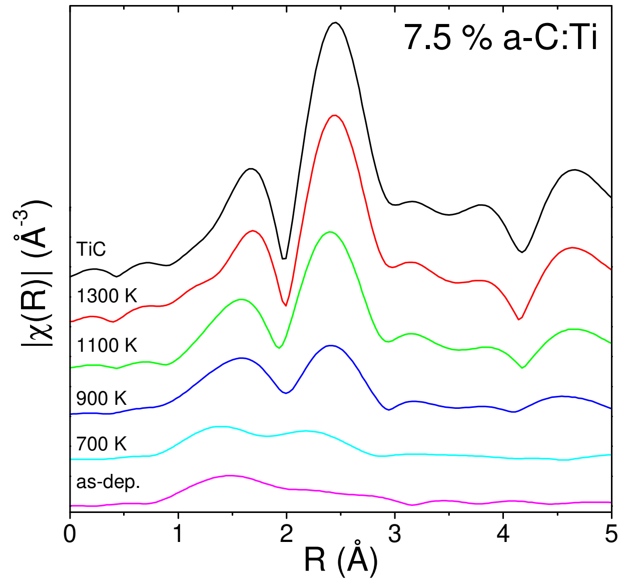

505

506

507 Fig. 9

508

509

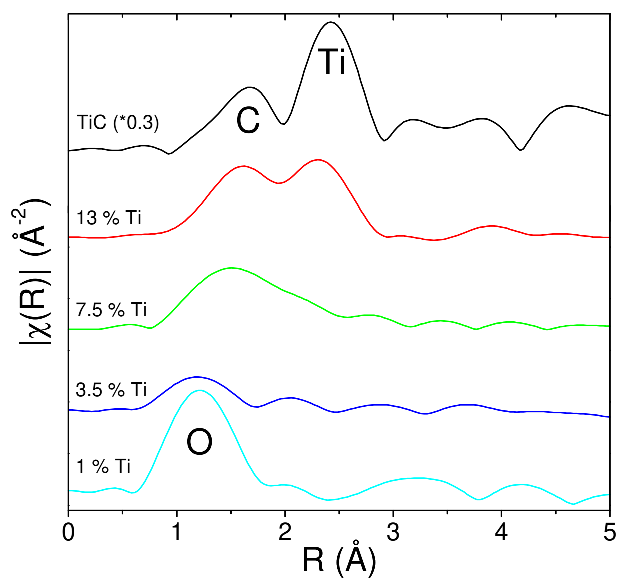

510

511 Fig. 10

512

513

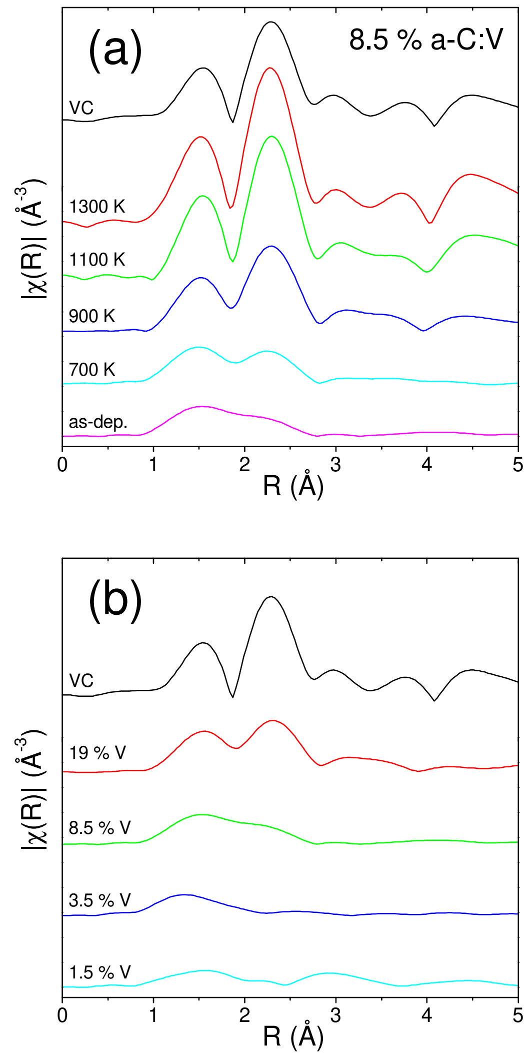

514

515 Fig. 11

516

517

518

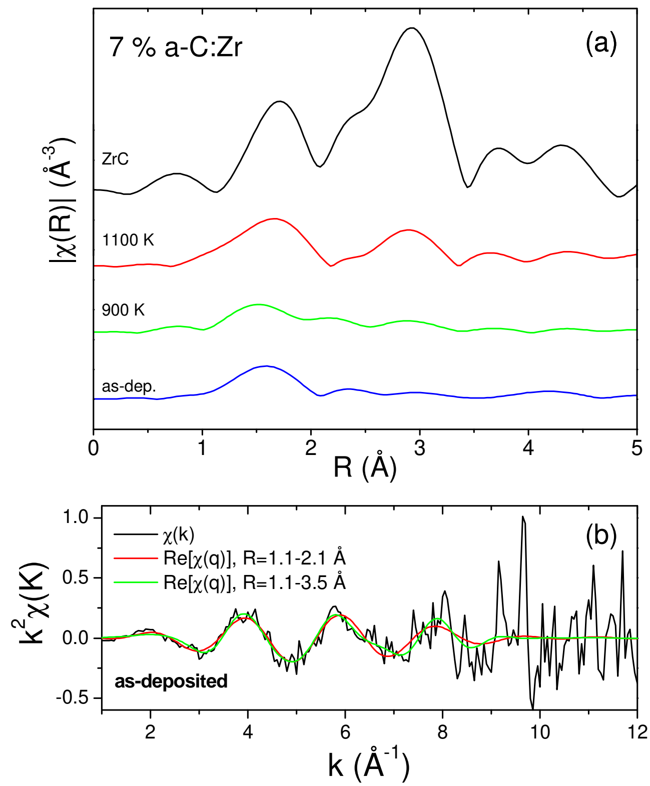

519

520 Fig. 12

521

522

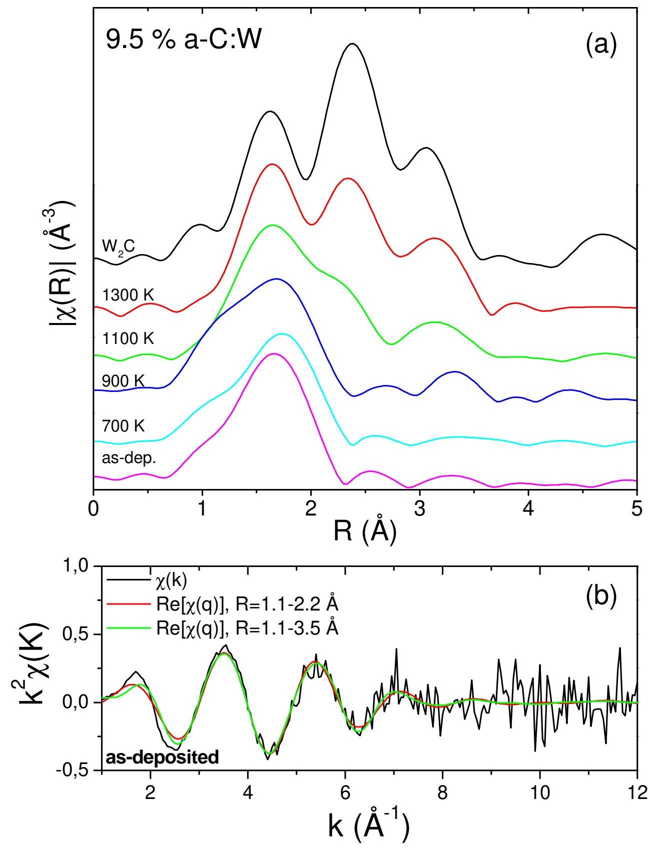

523

524

525 Fig. 13

526

527

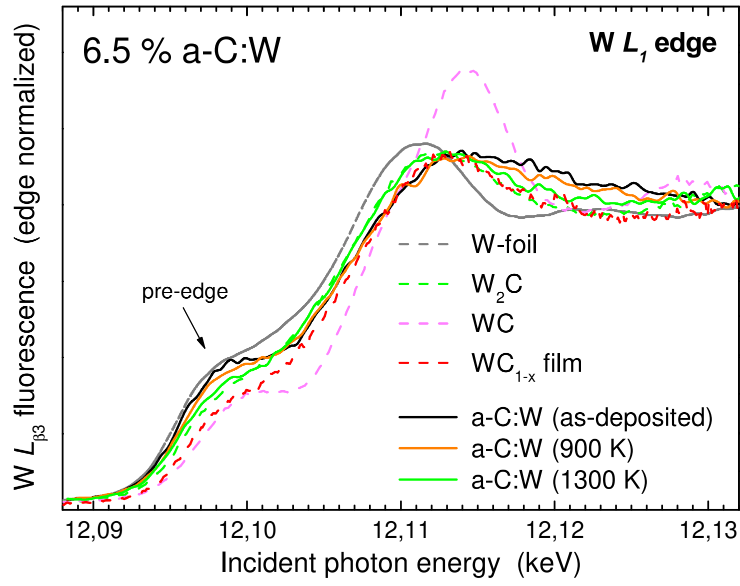

528

529 List of Figure Captions

530

531

532 Fig. 1: X-ray diffractograms of a) 7.5 % a-C:Ti, b) 8.5 % a-C:V, c) 7 % a-C:Zr films after
533 deposition and annealing up to 1300 K. Diffraction peaks for TiC, VC, and ZrC are indicated.

534

535 Fig. 2: Crystallite sizes for VC crystallites determined by XRD for a-C:V films with different
536 concentrations and annealing temperatures up to 1300 K. Crystallite sizes determined by
537 TEM are given for three samples. The errors represent the uncertainty introduced by the peak
538 fitting procedure (XRD) or the particle size distribution (TEM).

539

540 Fig. 3: TEM micrograph of a 1.5 % V containing a-C:V film after annealing to 1300 K.

541

542 Fig. 4: Carbide crystallite sizes in Ti, V, and Zr-doped carbon films with different metal
543 concentrations annealed to 900, 1100 and 1300 K. Note the logarithmic y-scale.

544

545 Fig. 5: X-ray diffractograms of 9.5 % a-C:W films after deposition and annealed up to 1300
546 K. Diffraction peaks for the carbide phases W_2C, WC and WC_{1-x} are shown, the used PDF
547 card numbers of the ICDD database are indicated.

548

549 Fig. 6: a) STEM bright field micrograph of a 9.5 % a-C:W sample, annealed up to 1300 K.
550 Electron diffraction of single particles revealed WC_{1-x} and W_2C phase. b) STEM Z contrast
551 micrograph of the same area as in a).

552

553 Fig. 7: a) Normalized Ti K-edge XAFS spectra of 7.5 % a-C:Ti films annealed up to 1300 K
554 and TiC standard. b) XANES region of the spectra in a). The inset shows the magnified
555 region of the pre-edge peak

556

557 Fig. 8: EXAFS data of the annealing series of the 7.5 % a-C:Ti sample, after Fourier
558 transformation of $k^2\chi(k)$, k=2-8.5 $Å^{-1}$, not phase shift corrected.

559

560 Fig. 9: EXAFS data of as-deposited a-C:Ti films with different Ti concentrations and the TiC
561 standard, after Fourier transformation of $k\chi(k)$, k=2-8.5 $Å^{-1}$, not phase shift corrected.

562

563 Fig. 10: a) EXAFS data of the annealing series of the 8.5 % a-C:V sample, after Fourier
564 transformation of $k^2\chi(k)$, k=2-8.5 $Å^{-1}$, not phase shift corrected. b) EXAFS data of as-
565 deposited a-C:V films with different V concentrations and the VC standard, after Fourier
566 transformation of $k^2\chi(k)$, k=2-8.5 $Å^{-1}$, not phase shift corrected.

567

568 Fig. 11 a) EXAFS data of the 7 % a-C:Zr sample after deposition and annealing to 900 and
569 1100 K, and a ZrC standard (after Fourier transformation of $k^2\chi(k)$, k=2.5-8.5 $Å^{-1}$, not phase
570 shift corrected). b) $\chi(k)$ of the as-deposited sample and backtransformed data for R = 1.1-2.1
571 Å (data range of the first shell) and R = 1.1-3.5 Å (data range of the first and second shell).

572

573 Fig. 12 a) EXAFS data of the 9.5 % a-C:W sample after deposition and annealed up to 1300
574 K, and a W_2C standard (after Fourier transformation of $k^2\chi(k)$, k=2-8.5 $Å^{-1}$, not phase shift
575 corrected). b) $k^2\chi(k)$ for the as-deposited sample and backtransformed data for R=1.1-2.2 Å
576 (data range of the first shell) and R= 1.1-3.5 Å (data range of the first and second shell).

577

578 Fig. 13: Normalized W L_1 edge NEXAFS spectra of as-deposited and annealed (900 K, 1300

579 K) 6.5 % a-C:W films and W standard materials.

580

581